

Research Article

Dual-Polarized Planar Phased Array Analysis for Meteorological Applications

Chen Pang,¹ Peter Hoogeboom,² François Le Chevalier,² Herman W. J. Russchenberg,² Jian Dong,¹ Tao Wang,¹ and Xuesong Wang¹

¹National University of Defense Technology, Deyu Road 109, Changsha 410073, China

²Delft University of Technology, Stevinweg 1, 2628 CD Delft, Netherlands

Correspondence should be addressed to Chen Pang; pangchen1017@hotmail.com

Received 27 February 2015; Revised 19 July 2015; Accepted 22 July 2015

Academic Editor: Stefano Selleri

Copyright © 2015 Chen Pang et al. This is an open access article distributed under the Creative Commons Attribution License, which permits unrestricted use, distribution, and reproduction in any medium, provided the original work is properly cited.

This paper presents a theoretical analysis for the accuracy requirements of the planar polarimetric phased array radar (PPPAR) in meteorological applications. Among many factors that contribute to the polarimetric biases, four factors are considered and analyzed in this study, namely, the polarization distortion due to the intrinsic limitation of a dual-polarized antenna element, the antenna pattern measurement error, the entire array patterns, and the imperfect horizontal and vertical channels. Two operation modes, the alternately transmitting and simultaneously receiving (ATSR) mode and the simultaneously transmitting and simultaneously receiving (STSR) mode, are discussed. For each mode, the polarimetric biases are formulated. As the STSR mode with orthogonal waveforms is similar to the ATSR mode, the analysis is mainly focused on the ATSR mode and the impacts of the bias sources on the measurement of polarimetric variables are investigated through Monte Carlo simulations. Some insights of the accuracy requirements are obtained and summarized.

1. Introduction

Recently, the weather radar community has paid much attention to the polarimetric phased array radar (PPAR) due to its agile electronic beam steering capability, which has the potential to significantly advance weather observations [1]. Various system designs have been presented and studied. A low cost mobile X-band phased array weather radar with phase-tilt antenna array was developed in [2]. Fulton and Chappell [3] designed an S-band, differentially probe-fed, stacked patch antenna for multifunctional phased array weather radar applications and studied the calibration method [4]. Zhang et al. [5] proposed a cylindrical configuration for the polarimetric phased array weather radar and illustrated the advantages of the cylindrical configuration over the planar configuration. In [6] an overview of the calibration techniques, tools, and challenges surrounding the development of a cylindrical polarimetric phased array radar (CPPAR) demonstrator was provided. The design of interleaved sparse arrays [7] for the agile polarization control was analyzed with the purpose

of meteorological applications. Dong et al. [8] analyzed the polarization characteristics of two ideal orthogonal Huygens sources and evaluated their polarimetry performance.

As shown in [1, 9], a high-accuracy measurement of polarimetric variables is required to provide meaningful information for reliable hydrometeor classifications and improved quantitative precipitation estimations. For example, it is desirable that the measurement error for the differential reflectivity Z_{DR} be on the order of 0.1 dB. In addition, it is desirable that the copolar correlation coefficient ρ_{hv} error be less than 0.01. In previous research [9–13], the polarimetric biases of weather radars with mechanically scanning antennas have been widely discussed. A detailed literature review of the bias analysis and calibration methods was presented in [9]. Generally, in order to make accurate polarimetric measurements by using a mechanically scanning antenna, a narrow beam with low sidelobes, low coaxial cross-polarization, and high polarization isolation are indispensable.

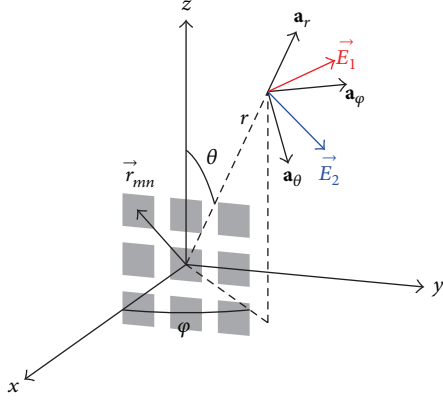


FIGURE 1: The array configuration and spherical coordinate system used for radiated electric fields.

Although the weather radar polarimetry has matured for years, there are some challenges for the planar polarimetric phased array radar (PPPAR) [14]. As shown in Figure 1, the array is placed on the yz plane. When the beam is away from the principle planes, the electric field \vec{E}_1 from the horizontal (H) port and \vec{E}_2 from the vertical (V) port are not necessarily orthogonal, which will introduce polarimetric biases that are not negligible. The nonorthogonality of the H and V polarizations is called the polarization distortion in this paper. Meanwhile, the polarization distortion also includes mismatches in the power levels of H and V beams as a function of the scan angle. The calibration matrix that relies on the measured array patterns is needed to calibrate the polarimetric bias due to the polarimetric distortion. As the measured antenna pattern always contains measurement errors, the calibration matrix cannot completely calibrate the bias due to the polarization distortion, which is not thoroughly analyzed in previous research [1, 15, 16] and will be discussed in this study. Moreover, in [1, 15, 16] it implies that the beam is thin enough so that the calibration performed at the boresight is sufficient to retrieve the polarimetric variables. However, in practice the finite beamwidth also contributes to the polarimetric bias, which will be evaluated in this paper. Besides the antenna, the imperfect H/V channels can still bias the polarimetric variables, which will be modeled and analyzed. Actually, other factors, such as the mismatch between element patterns, spatial variations of cross-polarization patterns, mutual coupling edge effects, diffracted fields, and surface waves, can significantly affect the overall accuracy of a PPPAR. To simplify the analysis, these factors are ignored.

Usually, there are two operation modes chosen for weather observations, the alternately transmitting and simultaneously receiving (ATSR) mode and the simultaneously transmitting and simultaneously receiving (STSR) mode. Each mode has its advantages and disadvantages. With a “perfect” antenna, the STSR mode is vastly superior to the ATSR mode in the worst-case polarimetric/spectral situations. Thus, the STSR mode is the preferred mode from a meteorological standpoint. However, both the theoretical

analysis and measurement experiments have shown that the STSR mode has higher accuracy requirements than the ATSR mode. This paper is mainly focused on the ATSR mode as it is simple for the analysis.

The remainder of this paper is organized as follows. Section 2 presents the array model. Sections 3 and 4 give the detailed analysis in the ATSR and STSR modes, respectively. Summaries and conclusions are made in Section 5.

2. Array Model

The coordinate system and array configuration are shown in Figure 1. It is common that in antenna measurements the antenna is placed on the xy plane. In this situation the H and V vectors correspond to the second definition in [17]. In this paper, the array with M rows and N columns is placed on the yz plane, which is different from the typical situation. The reason is that in meteorological applications when the array is placed on the yz plane, the expressions of the horizontal and vertical polarization basis are simple, which are written as

$$\begin{aligned} \mathbf{a}_h &= \mathbf{a}_\varphi, \\ \mathbf{a}_v &= -\mathbf{a}_\theta, \end{aligned} \quad (1)$$

where $\{\mathbf{a}_h, \mathbf{a}_v\}$ is the horizontal and so-called “vertical” polarization basis and \mathbf{a}_r , \mathbf{a}_θ , and \mathbf{a}_φ are unit vectors in the spherical coordinate system.

We consider the array has a 90° angular range in azimuth and a 30° range in elevation, which is applicable for weather observations. Thus, in Figure 1 φ is from -45° to 45° and θ is from 60° to 90° . For a well-designed array, it would be symmetrical with respect to φ . So in this paper we only consider φ from 0° to 45° and θ from 60° to 90° . Accordingly, the beam direction $(\theta_s, \varphi_s) = (90^\circ, 0^\circ)$ is the broadside of the array.

2.1. Element Pattern. The element pattern in a dual-polarized phased array can be written as

$$\mathbf{f}(\theta, \varphi) = \begin{bmatrix} f_{hh}(\theta, \varphi) & f_{hv}(\theta, \varphi) \\ f_{vh}(\theta, \varphi) & f_{vv}(\theta, \varphi) \end{bmatrix}, \quad (2)$$

where

- (i) $f_{hh}(\theta, \varphi)$ is the horizontal electric field component when only the H port is excited
- (ii) $f_{hv}(\theta, \varphi)$ is the horizontal electric field component when only the V port is excited
- (iii) $f_{vh}(\theta, \varphi)$ is the vertical electric field component when only the H port is excited
- (iv) $f_{vv}(\theta, \varphi)$ is the vertical electric field component when only the V port is excited.

For a practical dual-polarized antenna element, the cross-polarization components $f_{hv}(\theta, \varphi)$ and $f_{vh}(\theta, \varphi)$ are not 0 in the beam scan area.

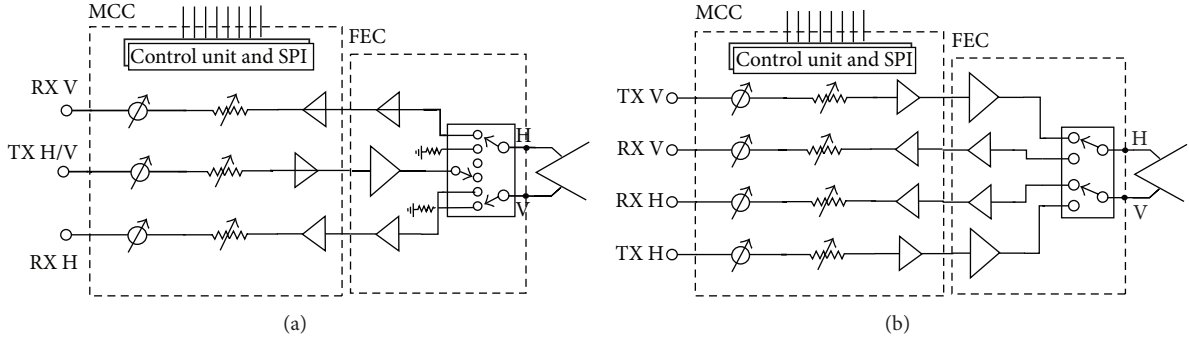


FIGURE 2: Dual-polarized T/R modules for polarimetric phased array weather radars. (a) is for the ATSR mode and (b) is for the STSR mode. In the ATSR mode, one channel is shared for transmitting H and V signals and two independent channels are used for reception. In the STSR mode, four independent channels, two for transmission, two for reception, and one T/R switch to commute the transmission and reception signals, are required.

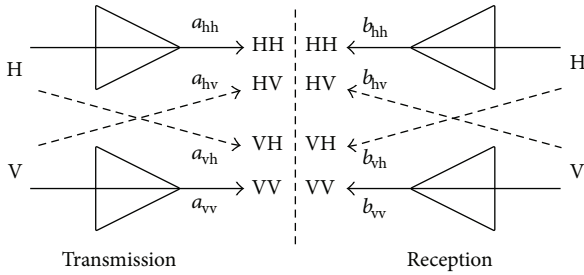


FIGURE 3: Channel imbalance and channel coupling.

2.2. Transmission and Reception Patterns. Figure 2 from [18] shows dual-polarized T/R modules for polarimetric phased array weather radars in the ATSR and STSR modes. As explained in [4], the T/R module connected to each element may have cross-coupling between its H and V channels as well as complex gain/phase imbalances. These cross-couplings and imbalances can be modeled by a matrix multiplication of the H and V signals presented to the T/R module on both transmission and reception with components as designated in Figure 3. In this paper, we use the term “channel isolation” to express the cross-coupling between the H and V channels. Meanwhile, we use the term “channel imbalance” to express complex gain/phase imbalances between the H and V channels.

For each element, we use a 2×2 complex matrix \mathbf{A} to model the channel imbalance and channel isolation for the transmission while \mathbf{B} is for the reception. \mathbf{A} and \mathbf{B} are written as

$$\mathbf{A} = \begin{bmatrix} a_{hh} & a_{hv} \\ a_{vh} & a_{vv} \end{bmatrix}, \quad (3)$$

$$\mathbf{B} = \begin{bmatrix} b_{hh} & b_{hv} \\ b_{vh} & b_{vv} \end{bmatrix}, \quad (4)$$

where a_{hh} , a_{vv} , b_{hh} , and b_{vv} describe the channel imbalance and a_{hv} , a_{vh} , b_{hv} , and b_{vh} give the channel isolation. For

simplicity, we assume $a_{hh} = b_{hh} = 1$. Then the channel imbalance CIM is defined as

$$\text{CIM} = \max \left\{ \left| 20 \log \frac{1}{|a_{vv}|} \right|, \left| 20 \log \frac{1}{|b_{vv}|} \right| \right\}. \quad (5)$$

Note that if $|a_{vv}| > 1$, there will be $20 \log(1/|a_{vv}|) < 0$. Thus we use the expression $|20 \log(1/|a_{vv}|)|$ such that CIM remains positive.

Similarly, the channel isolation CIS can be defined as

$$\text{CIS} = 20 \log \left(\max \left\{ \frac{1}{|a_{vh}|}, \frac{|a_{vv}|}{|a_{hv}|}, \frac{1}{|b_{vh}|}, \frac{|b_{vv}|}{|b_{hv}|} \right\} \right) \quad (6)$$

which means CIS is defined as the worst value among $1/|a_{vh}|$, $|a_{vv}|/|a_{hv}|$, $1/|b_{vh}|$, and $|b_{vv}|/|b_{hv}|$.

The array transmission pattern $\mathbf{T}(\theta, \varphi)$ and reception pattern $\mathbf{R}(\theta, \varphi)$ are expressed as [19]

$$\begin{aligned} \mathbf{T}(\theta, \varphi) &= \sum_{m=1}^M \sum_{n=1}^N X_{mn}(\theta_s, \varphi_s) \mathbf{f}_{mn}(\theta, \varphi) \cdot \mathbf{A}_{mn}, \\ \mathbf{R}(\theta, \varphi) &= \sum_{m=1}^M \sum_{n=1}^N Y_{mn}(\theta_s, \varphi_s) \mathbf{f}_{mn}(\theta, \varphi) \cdot \mathbf{B}_{mn}, \end{aligned} \quad (7)$$

where (θ_s, φ_s) is the beam direction. $X_{mn}(\theta_s, \varphi_s)$ and $Y_{mn}(\theta_s, \varphi_s)$ are weighting coefficients with respect to each element. \mathbf{A}_{mn} and \mathbf{B}_{mn} model the imperfect channel effects.

The mutual coupling between array elements is complicated so that a thorough analysis of the mutual coupling usually includes the full-wave electromagnetic computation and measurement experiments, which is beyond the scope of this paper. Moreover, for a large array, most of the elements are far from an edge. Therefore, except for the phase center displacement, all of the central element patterns are nearly the same. So it is reasonable to use the array average element pattern to replace the single element pattern. Hence, $\mathbf{T}(\theta, \varphi)$ and $\mathbf{R}(\theta, \varphi)$ reduce to

$$\mathbf{T}(\theta, \varphi) = \mathbf{f}_{\text{ave}}(\theta, \varphi) \mathbf{F}_T, \quad (8)$$

$$\mathbf{R}(\theta, \varphi) = \mathbf{f}_{\text{ave}}(\theta, \varphi) \mathbf{F}_R, \quad (9)$$

where $\mathbf{f}_{\text{ave}}(\theta, \varphi)$ is called the array average element pattern. The subscripts T and R in (8) and (9) represent the transmission and reception, respectively. \mathbf{F}_T and \mathbf{F}_R are written as

$$\mathbf{F}_T = \sum_{m=1}^M \sum_{n=1}^N \exp(jk\vec{r}_{mn} \cdot \mathbf{a}_r) X_{mn}(\theta_S, \varphi_S) \mathbf{A}_{mn}, \quad (10)$$

$$\mathbf{F}_R = \sum_{m=1}^M \sum_{n=1}^N \exp(jk\vec{r}_{mn} \cdot \mathbf{a}_r) Y_{mn}(\theta_S, \varphi_S) \mathbf{B}_{mn}.$$

3. Array Analysis in ATSR Mode

3.1. Formulation. For a point target with the polarization scattering matrix (PSM) \mathbf{S} in the direction (θ, φ) at the range r , the received voltage matrix can be written as

$$\mathbf{V} = C \frac{\exp(-j2kr)}{4\pi r^2} \mathbf{R}^t \cdot \mathbf{S} \cdot \mathbf{T} \cdot \mathbf{E}_{\text{ATSR}}^{\text{inc}}, \quad (11)$$

where C is a gain term. Here the superscript “ t ” means matrix transpose. $k = 2\pi/\lambda$ and λ is the wavelength. $\mathbf{E}_{\text{ATSR}}^{\text{inc}}$ is the unit excitation for H and V ports, which is written as

$$\mathbf{E}_{\text{ATSR}}^{\text{inc}} = \begin{bmatrix} 1 & 0 \\ 0 & 1 \end{bmatrix}. \quad (12)$$

The received voltage matrix for distributed precipitations can be expressed as an integral. Consider

$$\mathbf{V} = \int_{\Omega} \mathbf{R}^t(\theta, \varphi) \cdot \mathbf{S}(\theta, \varphi) \cdot \mathbf{T}(\theta, \varphi) d\Omega, \quad (13)$$

where Ω is the solid angle and $d\Omega = \sin\theta d\theta d\varphi$. In (13), the gain term C and the term related to range r are dropped for the sake of simplicity. To retrieve $\mathbf{S}(\theta, \varphi)$, the calibrated voltage matrix can be expressed as

$$\hat{\mathbf{V}} = \mathbf{C}_R \cdot \mathbf{V} \cdot \mathbf{C}_T = \int_{\Omega} \mathbf{C}_R \cdot \mathbf{R}^t \cdot \mathbf{S} \cdot \mathbf{T} \cdot \mathbf{C}_T d\Omega, \quad (14)$$

where the calibration matrices \mathbf{C}_T and \mathbf{C}_R are expressed as

$$\begin{aligned} \mathbf{C}_T &= \left(\mathbf{T}(\theta, \varphi) \right)_{\theta=\theta_S, \varphi=\varphi_S}^{-1}, \\ \mathbf{C}_R &= \left(\mathbf{R}^t(\theta, \varphi) \right)_{\theta=\theta_S, \varphi=\varphi_S}^{-1}. \end{aligned} \quad (15)$$

\mathbf{C}_T and \mathbf{C}_R can be obtained through array pattern measurements. By defining

$$\hat{\mathbf{R}} = \mathbf{R} \cdot (\mathbf{C}_R)^t = \begin{bmatrix} \hat{R}_{hh} & \hat{R}_{hv} \\ \hat{R}_{vh} & \hat{R}_{vv} \end{bmatrix}, \quad (16)$$

$$\hat{\mathbf{T}} = \mathbf{T} \cdot \mathbf{C}_T = \begin{bmatrix} \hat{T}_{hh} & \hat{T}_{hv} \\ \hat{T}_{vh} & \hat{T}_{vv} \end{bmatrix},$$

the calibrated voltage matrix is written as

$$\hat{\mathbf{V}} = \int_{\Omega} \hat{\mathbf{R}}^t \cdot \mathbf{S} \cdot \hat{\mathbf{T}} d\Omega. \quad (17)$$

Assuming

$$\mathbf{S}(\theta, \varphi) = \begin{bmatrix} S_{hh}(\theta, \varphi) & 0 \\ 0 & S_{vv}(\theta, \varphi) \end{bmatrix} \quad (18)$$

the intrinsic differential reflectivity Z_{DR} is defined as

$$Z_{\text{DR}} = 10 \log \frac{\langle |S_{hh}|^2 \rangle}{\langle |S_{vv}|^2 \rangle}, \quad (19)$$

where $\langle \cdot \rangle$ means the ensemble average. The bias of Z_{DR} can be calculated as

$$Z_{\text{DR}}^b = 10 \log \frac{P_{hh}}{P_{vv}} - Z_{\text{DR}}, \quad (20)$$

where P_{ij} ($i, j = h, v$) is the received power. Meanwhile, the integrated cross-polarization ratio (ICPR) is calculated as

$$\text{ICPR} = 10 \log \frac{P_{vh}}{P_{hh}} \quad (21)$$

which is the minimal linear depolarization ratio L_{DR} that can be measured by a weather radar. After some trivial mathematical derivations, we get

$$Z_{\text{DR}}^b = 10 \log \frac{1 + W_1 Z_{\text{dr}}^{-1/2}}{W_2 + W_3 Z_{\text{dr}}^{1/2}}, \quad (22)$$

$$\text{ICPR} = 10 \log \frac{W_4 + W_5 Z_{\text{dr}}^{-1} + W_6 Z_{\text{dr}}^{-1/2}}{1 + W_1 Z_{\text{dr}}^{-1/2}},$$

where

$$\rho_{hv} \exp(j\phi_{\text{DP}}) = \frac{\langle S_{hh}^* S_{vv} \rangle}{\sqrt{\langle |S_{hh}|^2 \rangle \langle |S_{vv}|^2 \rangle}}, \quad (23)$$

$$W_1 = \frac{\int_{\Omega} 2\text{Re}(\hat{T}_{vh} \hat{R}_{vh} \hat{T}_{hh}^* \hat{R}_{hh}^* \rho_{hv} \exp(j\phi_{\text{DP}})) d\Omega}{\int_{\Omega} |T_{hh}|^2 |R_{hh}|^2 d\Omega}, \quad (24)$$

$$W_2 = \frac{\int_{\Omega} |\hat{T}_{vv}|^2 |\hat{R}_{vv}|^2 d\Omega}{\int_{\Omega} |T_{hh}|^2 |R_{hh}|^2 d\Omega}, \quad (25)$$

$$W_3 = \frac{\int_{\Omega} 2\text{Re}(\hat{T}_{vv} \hat{R}_{vv} \hat{T}_{hv} \hat{R}_{hv}^* \rho_{hv} \exp(j\phi_{\text{DP}})) d\Omega}{\int_{\Omega} |T_{hh}|^2 |R_{hh}|^2 d\Omega}, \quad (26)$$

$$W_4 = \frac{\int_{\Omega} |T_{hh}|^2 |R_{hv}|^2 d\Omega}{\int_{\Omega} |T_{hh}|^2 |R_{hh}|^2 d\Omega}, \quad (27)$$

$$W_5 = \frac{\int_{\Omega} |T_{vh}|^2 |R_{vv}|^2 d\Omega}{\int_{\Omega} |T_{hh}|^2 |R_{hh}|^2 d\Omega}, \quad (28)$$

$$W_6 = \frac{\int_{\Omega} 2\text{Re}(\hat{T}_{vh} \hat{R}_{vv} \hat{T}_{hh}^* \hat{R}_{hh}^* \rho_{hv} \exp(j\phi_{\text{DP}})) d\Omega}{\int_{\Omega} |T_{hh}|^2 |R_{hh}|^2 d\Omega}. \quad (29)$$

In (23) ρ_{hv} is called the copolar correlation coefficient and ϕ_{DP} represents the differential phase. The symbol * means complex conjugate.

According to (22), it is clear that Z_{DR}^b and ICPR are related to both the array patterns and the intrinsic Z_{dr} . The impacts of Z_{dr} and $\rho_{hv} \exp(j\phi_{DP})$ on Z_{DR}^b have been thoroughly analyzed in [9] and those conclusions can be directly applied for the analysis of a PPPAR. Hence, in this paper we assume $Z_{dr} = 1$ and $\rho_{hv} \exp(j\phi_{DP}) = 1$ so that we can focus on the biases due to the radar system.

3.2. Array with Perfect H/V Channels. An array with perfect H/V channels means that the channel imbalance and isolation can be ignored. Hence, the transmission and reception patterns can be written as

$$\begin{aligned} \mathbf{T}(\theta, \varphi) &= \mathbf{f}_{ave}(\theta, \varphi) \sum_{m=1}^M \sum_{n=1}^N \exp(jk\vec{r}_{mn} \cdot \mathbf{a}_r) X_{mn}(\theta_S, \varphi_S), \\ \mathbf{R}(\theta, \varphi) &= \mathbf{f}_{ave}(\theta, \varphi) \sum_{m=1}^M \sum_{n=1}^N \exp(jk\vec{r}_{mn} \cdot \mathbf{a}_r) Y_{mn}(\theta_S, \varphi_S). \end{aligned} \quad (30)$$

For the transmission pattern, the radiation power is principal. Thus, a uniform illumination is applied. For the reception pattern, a beam with low sidelobes is desired. Here, we choose the Taylor weighting. So $\hat{\mathbf{R}}$ and $\hat{\mathbf{T}}$ are written as

$$\begin{aligned} \hat{\mathbf{T}} &= \mathbf{T} \cdot \mathbf{C}_T = F_{uni}(\theta, \varphi) \mathbf{f}_{ave}(\theta, \varphi) \cdot \mathbf{C}_T, \\ \hat{\mathbf{R}} &= \mathbf{R} \cdot (\mathbf{C}_R)^t = F_{tay}(\theta, \varphi) \mathbf{f}_{ave}(\theta, \varphi) \cdot (\mathbf{C}_R)^t, \end{aligned} \quad (31)$$

where $F_{uni}(\theta, \varphi)$ and $F_{tay}(\theta, \varphi)$ are the array factors of the uniform and Taylor weightings. According to the definitions of \mathbf{C}_T and \mathbf{C}_R , $\hat{\mathbf{T}}$ and $\hat{\mathbf{R}}$ can be modeled as

$$\hat{\mathbf{T}} = \hat{F}_{uni} \begin{bmatrix} 1 + \varepsilon_{hh}^T(\theta, \varphi) & \varepsilon_{hv}^T(\theta, \varphi) \\ \varepsilon_{vh}^T(\theta, \varphi) & 1 + \varepsilon_{vv}^T(\theta, \varphi) \end{bmatrix}, \quad (32)$$

$$\hat{\mathbf{R}} = \hat{F}_{tay} \begin{bmatrix} 1 + \varepsilon_{hh}^R(\theta, \varphi) & \varepsilon_{hv}^R(\theta, \varphi) \\ \varepsilon_{vh}^R(\theta, \varphi) & 1 + \varepsilon_{vv}^R(\theta, \varphi) \end{bmatrix}, \quad (33)$$

where ε_{ij} are the error terms after the calibration. \hat{F}_{uni} and \hat{F}_{tay} are the normalized array factors. The superscripts T and R represent the transmission and reception, which are usually dropped for simplicity. To simplify the analysis, ε_{ij} is modeled as

$$\varepsilon_{ij}(\theta, \varphi) \approx \alpha_{ij}(\theta - \theta_S) + \beta_{ij}(\varphi - \varphi_S) + \delta_{ij}, \quad (34)$$

where α_{ij} , β_{ij} , and δ_{ij} are complex numbers. The unit of θ and φ is radian. If \mathbf{C}_T and \mathbf{C}_R have no error, there will be $\varepsilon_{ij} = 0$ at (θ_S, φ_S) ; that is, $\delta_{ij} = 0$. However, due to the antenna pattern measurement errors, δ_{ij} is not 0. In addition, α_{ij} and β_{ij} indicate the polarization variation near (θ_S, φ_S) .

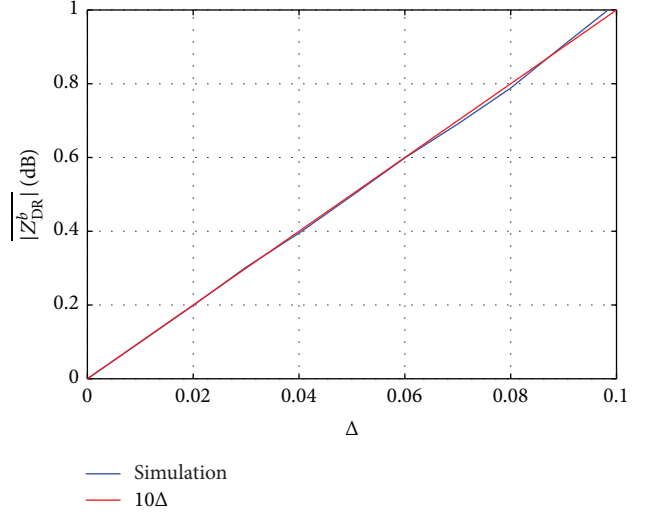


FIGURE 4: The relation between Δ and $|Z_{DR}^b|$.

It should be pointed out that the linear error model (34) is most appropriate for well-behaved elements making up an array that is large enough to ensure that it is accurate over the beamwidth of the overall array.

According to Appendix, we know that the upper bound of δ_{ij} has the same level as the relative error upper bound E_f of the antenna measurements. Therefore, in the rest of this paper we just focus on δ_{ij} .

First, we analyze a simple case to get some insights towards δ_{ij} . We assume there is only one spherical scatterer in the beam direction (θ_S, φ_S) , indicating $Z_{DR} = 0$ dB and $L_{DR} = -\infty$ dB. So we can ignore the impacts of the finite beamwidth and sidelobes. Consequently, Z_{DR}^b can be calculated as

$$Z_{DR}^b = 20 \log \left| \frac{1 + \delta_{hh}^T + \delta_{hh}^R + \delta_{hh}^T \delta_{hh}^R + \delta_{vh}^T \delta_{vh}^R}{1 + \delta_{vv}^T + \delta_{vv}^R + \delta_{vv}^T \delta_{vv}^R + \delta_{hv}^T \delta_{hv}^R} \right|. \quad (35)$$

Furthermore, we assume $|\delta_{ij}| = \Delta$ and the phase of δ_{ij} is uniformly distributed in $[0, 2\pi]$. Using Taylor expansion and ignoring the second and higher order terms, we can get the approximation of the average bias of $|Z_{DR}^b|$:

$$\overline{|Z_{DR}^b|} \approx 10\Delta, \quad (36)$$

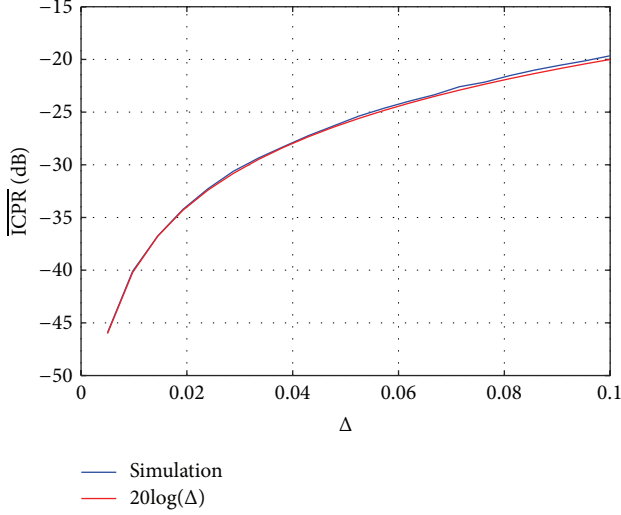
where $\bar{\cdot}$ means mathematical expectation. Since Z_{DR}^b has a symmetric distribution centered at 0, there is $\overline{Z_{DR}^b} = 0$. Hence, we use $\overline{|Z_{DR}^b|}$ other than $\overline{Z_{DR}^b}$. Figure 4 shows the relation between Δ and $\overline{|Z_{DR}^b|}$. The red line is calculated from (36) while the blue line is obtained through Monte Carlo simulation in which δ_{ij}^T and δ_{ij}^R are generated from a random number generator and Z_{DR}^b is calculated from (35). In Figure 4 we see that the approximation from (36) agrees well with the result from Monte Carlo simulation.

Using the same procedure, the average ICPR is derived in (37). Figure 5 shows the relation between Δ and $\overline{\text{ICPR}}$:

$$\overline{\text{ICPR}} \approx 20 \log(\Delta). \quad (37)$$

TABLE 1: Array parameters.

Array size	64×64
Elements separation	$\lambda/2$
Sidelobe level of F_{tay}	-40 dB

FIGURE 5: The relation between Δ and $\overline{\text{ICPR}}$.

From Figures 4 and 5, we know that the calibration error δ_{ij} has great impacts on Z_{DR}^b and ICPR. For a single spherical scatterer, to achieve $|Z_{\text{DR}}^b| < 0.1$ dB, Δ should be less than 0.01, which is really demanding for antenna pattern measurements. Moreover, we see that the relation between Δ and $|Z_{\text{DR}}^b|$ is linear while the relation between Δ and $\overline{\text{ICPR}}$ is logarithmic.

As revealed in [9, 12, 13], the finite beamwidth has considerable impacts on the measurement of polarimetric variables. In order to evaluate the bias under different conditions, a method based on Monte Carlo simulation is developed so that we can evaluate the polarimetric bias with different parameters. The array parameters are shown in Table 1. The simulation procedure is shown below.

Step 1. Specify the polarization distortion calibration error $|\delta_{ij}|$.

Step 2. Generate α_{ij} , β_{ij} , and δ_{ij} through a random number generator.

Step 3. Calculate $\hat{\mathbf{T}}$ from (32) and $\hat{\mathbf{R}}$ from (33).

Step 4. Calculate $\hat{\mathbf{V}}$ from (17).

Step 5. Calculate Z_{DR}^b from (20) and ICPR from (21).

The simulation parameters are listed in Table 2. $U(a, b)$ means the uniform distribution in $[a, b]$ and $\text{Arg}(z)$ represents the phase of z . It should be pointed out that a -40 dB Taylor weighting is not practical for the implementation.

TABLE 2: Simulation parameters.

Z_{DR}	0 dB
L_{DR}	$-\infty$ dB
$ \delta_{ij} $	0.01
$ \alpha_{ij} $	$U(0, 2)$
$ \beta_{ij} $	$U(0, 2)$
$\text{Arg}(\alpha_{ij})$	$U(0, 2\pi)$
$\text{Arg}(\beta_{ij})$	$U(0, 2\pi)$
$\text{Arg}(\delta_{ij})$	$U(0, 2\pi)$

TABLE 3: The model parameters of a pair of crossed dipoles in the beam direction ($60^\circ, 45^\circ$).

	α	β	δ	R^2
ε_{hh}	0.0000	-1.1092	-0.0013	0.99
ε_{hv}	0	0	0	None
ε_{vh}	1.1526	-0.4989	0.0007	0.99
ε_{vv}	0.5769	0.0000	-0.0013	0.99

According to [14], for weather observations the two-way sidelobe level of a PPPAR is expected to be under -54 dB which is equal to that of the WSR-88D. Thus the simulated results with a -13 dB uniform weighting and -40 dB Taylor weighting are more comparable to those of radars with mechanical scanning antennas.

The ranges of α_{ij} and β_{ij} in Table 2 are determined based on the radiation pattern of a pair of crossed dipoles, which is written as

$$\mathbf{f}_{\text{dipole}}(\theta, \varphi) = \begin{bmatrix} \cos \varphi & 0 \\ \cos \theta \sin \varphi & \sin \theta \end{bmatrix}. \quad (38)$$

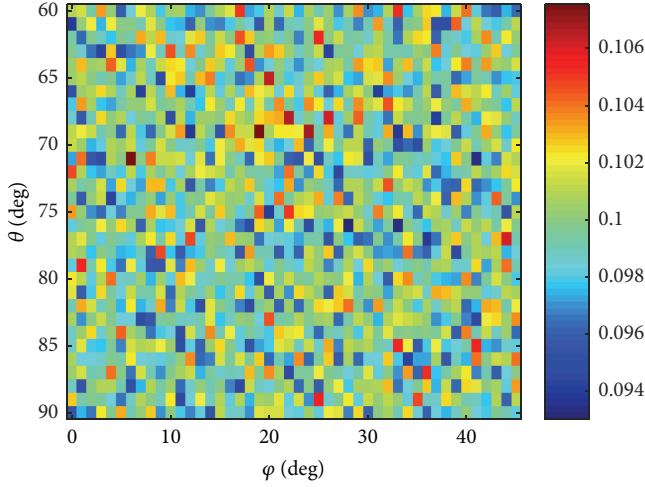
The calibrated pattern $\hat{\mathbf{f}}_{\text{dipole}}(\theta, \varphi)$ is then written as

$$\begin{aligned} \hat{\mathbf{f}}_{\text{dipole}}(\theta, \varphi) &= \begin{bmatrix} \cos \varphi & 0 \\ \cos \theta \sin \varphi & \sin \theta \end{bmatrix} \\ &\quad \cdot \begin{bmatrix} \cos \varphi_s & 0 \\ \cos \theta_s \sin \varphi_s & \sin \theta_s \end{bmatrix}^{-1} \\ &\equiv \begin{bmatrix} 1 + \varepsilon_{\text{hh}}(\theta, \varphi) & \varepsilon_{\text{hv}}(\theta, \varphi) \\ \varepsilon_{\text{vh}}(\theta, \varphi) & 1 + \varepsilon_{\text{vv}}(\theta, \varphi) \end{bmatrix}. \end{aligned} \quad (39)$$

Choosing $(\theta_s, \varphi_s) = (60^\circ, 45^\circ)$, we calculate $\varepsilon_{ij}(\theta, \varphi)$. By using Matlab Curve Fitting Toolbox, we calculate the parameters α_{ij} , β_{ij} , and δ_{ij} and show them in Table 3. R^2 is called the coefficient of determination, which is a number that indicates how well data fit a statistical model. As shown in Table 3, R^2 with respect to ε_{ij} is 0.99, indicating a very good approximation performance of the linear error model. According to Table 3, we know $\alpha_{ij}, \beta_{ij} \sim U(0, 2)$ is valid. Using the same procedure, we calculate the parameters α_{ij} , β_{ij} , and δ_{ij} for a pair of crossed dipoles with the length of λ and show them in Table 4. Actually, the practical phased array usually has an element spacing of about $\lambda/2$. Thus the ranges of α_{ij}

TABLE 4: The model parameters of a pair of crossed dipoles with the length of λ in the beam direction ($60^\circ, 45^\circ$).

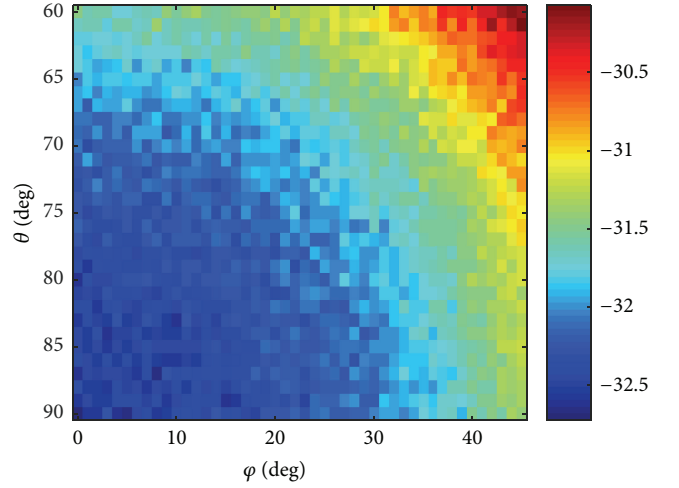
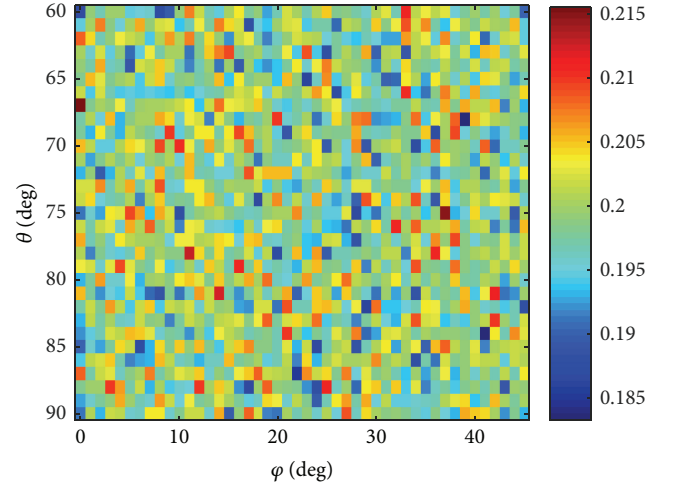
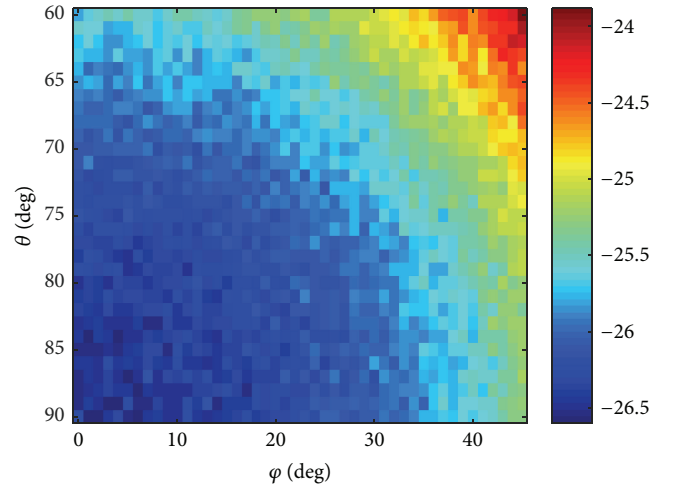
	α	β	δ	R^2
ϵ_{hh}	-1.0078	-2.7556	0.0076	0.99
ϵ_{hv}	0	0	0	None
ϵ_{vh}	-2.5394	-0.3672	0.0003	0.99
ϵ_{vv}	2.3362	0.0000	-0.0010	0.99

FIGURE 6: $|Z_{DR}^b|$ in dB with $|\delta_{ij}| = 0.01, |\alpha_{ij}|, |\beta_{ij}| \sim U(0, 2)$.

and β_{ij} should be better than the worst value in Table 4. In this paper, we assume $|\alpha_{ij}| < 4$ and $|\beta_{ij}| < 4$.

Figures 6 and 7 show the simulated $|Z_{DR}^b|$ and $\overline{\text{ICPR}}$ in the beam scan area $[60^\circ, 90^\circ] \times [0^\circ, 45^\circ]$. In Figure 6 most of $|Z_{DR}^b|$ are between 0.095 dB and 0.105 dB, which agrees with the approximation of (36). Figure 6 indicates that the impact of the finite beamwidth on Z_{DR}^b is not obvious and Z_{DR}^b is not sensitive to the beam expansion due to the beam scan. On the contrary, in Figure 7 the impact of the beam expansion on $\overline{\text{ICPR}}$ is obvious, with about a 2.5 dB difference between the broadside and the beam direction ($60^\circ, 45^\circ$). Furthermore, the ICPR of -32.6 dB at the broadside in Figure 7 is much larger than that of -40 dB calculated from (37), indicating that the finite beamwidth considerably affects the measurement of L_{DR} .

We then set $|\delta_{ij}| = 0.02, |\alpha_{ij}|, |\beta_{ij}| \in U(0, 4)$ and keep other parameters the same as those in Tables 1 and 2. Figures 8 and 9 show the simulation results. In Figure 8, most of $|Z_{DR}^b|$ are between 0.19 dB and 0.21 dB, which also agrees with (36) very well. In Figure 9, the difference between the broadside and the beam direction ($60^\circ, 45^\circ$) is about 2.5 dB and the minimal ICPR at the broadside ($90^\circ, 0^\circ$) is about -26.5 dB, increasing by about 7.5 dB compared with that calculated from the approximation of (37).

FIGURE 7: $\overline{\text{ICPR}}$ in dB with $|\delta_{ij}| = 0.01, |\alpha_{ij}|, |\beta_{ij}| \sim U(0, 2)$.FIGURE 8: $|Z_{DR}^b|$ in dB with $|\delta_{ij}| = 0.02, |\alpha_{ij}|, |\beta_{ij}| \sim U(0, 4)$.FIGURE 9: $\overline{\text{ICPR}}$ in dB with $|\delta_{ij}| = 0.02, |\alpha_{ij}|, |\beta_{ij}| \sim U(0, 4)$.

3.3. *Array with Imperfect H/V Channels.* With imperfect H/V channels, $\widehat{\mathbf{R}}$ and $\widehat{\mathbf{T}}$ can be written as

$$\begin{aligned}\widehat{\mathbf{T}}(\theta, \varphi) &= \begin{bmatrix} 1 + \varepsilon_{hh}^T & \varepsilon_{hv}^T \\ \varepsilon_{vh}^T & 1 + \varepsilon_{vv}^T \end{bmatrix} \widehat{\mathbf{F}}_T, \\ \widehat{\mathbf{R}}(\theta, \varphi) &= \begin{bmatrix} 1 + \varepsilon_{hh}^R & \varepsilon_{hv}^R \\ \varepsilon_{vh}^R & 1 + \varepsilon_{vv}^R \end{bmatrix} \widehat{\mathbf{F}}_R.\end{aligned}\quad (40)$$

\mathbf{A} and \mathbf{B} are expressed as

$$\begin{aligned}\mathbf{A} &= \begin{bmatrix} 1 & \eta_{hv} \exp(j\gamma_{hv}) \\ \eta_{vh} \exp(j\gamma_{vh}) & \eta_{vv} \exp(j\gamma_{vv}) \end{bmatrix}, \\ \mathbf{B} &= \begin{bmatrix} 1 & \tau_{hv} \exp(j\psi_{hv}) \\ \tau_{vh} \exp(j\psi_{vh}) & \tau_{vv} \exp(j\psi_{vv}) \end{bmatrix}.\end{aligned}\quad (41)$$

First, we analyze the case with a single spherical scatterer in the beam direction (θ_S, φ_S) . Thus we just need to consider $\widehat{\mathbf{T}}(\theta, \varphi)|_{\theta=\theta_S, \varphi=\varphi_S}$ and $\widehat{\mathbf{R}}(\theta, \varphi)|_{\theta=\theta_S, \varphi=\varphi_S}$. Since $X_{mn}(\theta_S, \varphi_S)$ and $Y_{mn}(\theta_S, \varphi_S)$ compensate the phase displacement $\exp(jk\bar{r}_{mn} \cdot \mathbf{a}_r)$, we can get

$$\begin{aligned}\widehat{\mathbf{T}}(\theta_S, \varphi_S) &= \begin{bmatrix} 1 + \delta_{hh}^T & \delta_{hv}^T \\ \delta_{vh}^T & 1 + \delta_{vv}^T \end{bmatrix} \\ &\quad \cdot \sum_{m=1}^M \sum_{n=1}^N |\widehat{X}_{mn}(\theta_S, \varphi_S)| \mathbf{A}_{mn}, \\ \widehat{\mathbf{R}}(\theta_S, \varphi_S) &= \begin{bmatrix} 1 + \delta_{hh}^R & \delta_{hv}^R \\ \delta_{vh}^R & 1 + \delta_{vv}^R \end{bmatrix} \\ &\quad \cdot \sum_{m=1}^M \sum_{n=1}^N |\widehat{Y}_{mn}(\theta_S, \varphi_S)| \mathbf{B}_{mn}.\end{aligned}\quad (42)$$

As $\sum_{m=1}^M \sum_{n=1}^N |\widehat{X}_{mn}(\theta_S, \varphi_S)| = 1$ and $\sum_{m=1}^M \sum_{n=1}^N |\widehat{Y}_{mn}(\theta_S, \varphi_S)| = 1$, the double summations on the right sides of (42) are close to the mathematical expectations of \mathbf{A} and \mathbf{B} . If $\gamma_{hv}, \gamma_{vh}, \psi_{hv}, \psi_{vh} \sim U(0, 2\pi)$, we have $\bar{a}_{hv} = 0, \bar{a}_{vh} = 0, \bar{b}_{hv} = 0$, and $\bar{b}_{vh} = 0$. In this situation, Z_{DR}^b can be calculated as

$$\begin{aligned}Z_{\text{DR}}^b &= 20 \log \left| \frac{1}{\bar{a}_{vv} \bar{b}_{vv}} \right| \left| \frac{1 + \delta_{hh}^T + \delta_{hh}^R + \delta_{hh}^T \delta_{hh}^R + \delta_{vh}^T \delta_{vh}^R}{1 + \delta_{vv}^T + \delta_{vv}^R + \delta_{vv}^T \delta_{vv}^R + \delta_{hv}^T \delta_{hv}^R} \right|. \quad (43)\end{aligned}$$

If $\delta_{ij}^T = \delta_{ij}^R = 0$, (43) reduces to

$$Z_{\text{DR}}^b = 20 \log \left| \frac{1}{\bar{a}_{vv} \bar{b}_{vv}} \right|. \quad (44)$$

Assuming $|a_{vv}| = |b_{vv}| < 1$, based on the definition of CIM in (5), (44) can be expressed as

$$Z_{\text{DR}}^b = 2\text{CIM}. \quad (45)$$

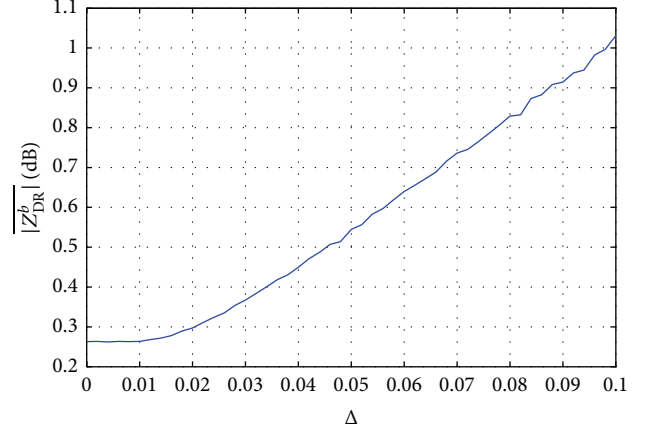


FIGURE 10: $|Z_{\text{DR}}^b|$ of a single spherical scatterer with imperfect H/V channels.

Figure 10 shows the simulated $|Z_{\text{DR}}^b|$ of a single spherical scatterer based on (43), in which $\eta_{vv} = \tau_{vv} = 0.99$, $\gamma_{vv}, \psi_{vv} \sim U(-10^\circ, 10^\circ)$, $\eta_{hv} = \eta_{vh} = \tau_{hv} = \tau_{vh} = 0$, $|\delta_{ij}| = \Delta$, and $\text{Arg}(\delta_{ij}) \sim U(0, 2\pi)$. In Figure 10 when $\Delta < 0.01$, $|Z_{\text{DR}}^b|$ almost remains constant around 0.26 dB and when $\Delta > 0.02$, $|Z_{\text{DR}}^b|$ increases linearly with a slope less than 10. When Δ is small the channel imbalance has the main contribution to Z_{DR}^b . Otherwise, the polarization distortion calibration error is the dominant bias source.

In order to evaluate the bias under different conditions, we use the Monte Carlo simulation method again, which is shown below.

Step 1. Specify $|\delta_{ij}|$.

Step 2. Generate α_{ij} , β_{ij} , and δ_{ij} from a random number generators and then calculate ε_{ij} .

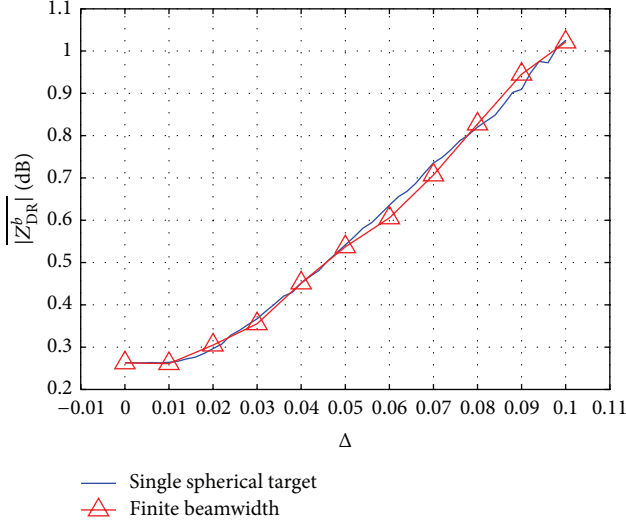
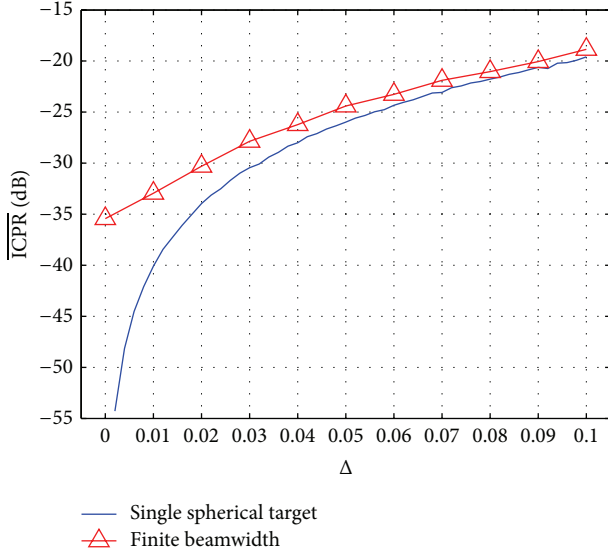
Step 3. Generate \mathbf{A}_{mn} and \mathbf{B}_{mn} for each element.

Step 4. Calculate $\widehat{\mathbf{R}}$ and $\widehat{\mathbf{T}}$.

Step 5. Calculate Z_{DR}^b and ICPR.

Figures 11 and 12 show simulated $|Z_{\text{DR}}^b|$ and $\overline{\text{ICPR}}$ in the beam direction $(90^\circ, 0^\circ)$, in which $|\alpha_{ij}| = |\beta_{ij}| = 2$, $\eta_{hv} = \eta_{vh} = \tau_{hv} = \tau_{vh} = 0$, $\eta_{vv}, \tau_{vv} \sim N(0.99, 0.01^2)$, and $\gamma_{vv}, \psi_{vv} \sim U(-10^\circ, 10^\circ)$. In Figure 11, the results with the finite beamwidth match the results of a single spherical scatterer well. However, Figure 12 indicates the finite beamwidth considerably affects ICPR when Δ is small.

We then set $\eta_{hv}, \eta_{vh}, \tau_{hv}, \tau_{vh} \sim N(0.01, 0.01^2)$, $\gamma_{hv}, \gamma_{vh}, \psi_{hv}, \psi_{vh} \sim U(-10^\circ, 10^\circ)$ and keep other parameters the same as those in Figures 11 and 12 to evaluate the impact of the channel isolation. The simulated $|Z_{\text{DR}}^b|$ and $\overline{\text{ICPR}}$ considering the imperfect channel isolation are given in Figures 13 and 14 with the blue squares while the simulated $|Z_{\text{DR}}^b|$ and $\overline{\text{ICPR}}$ from Figures 11 and 12 are still shown with the red triangles.

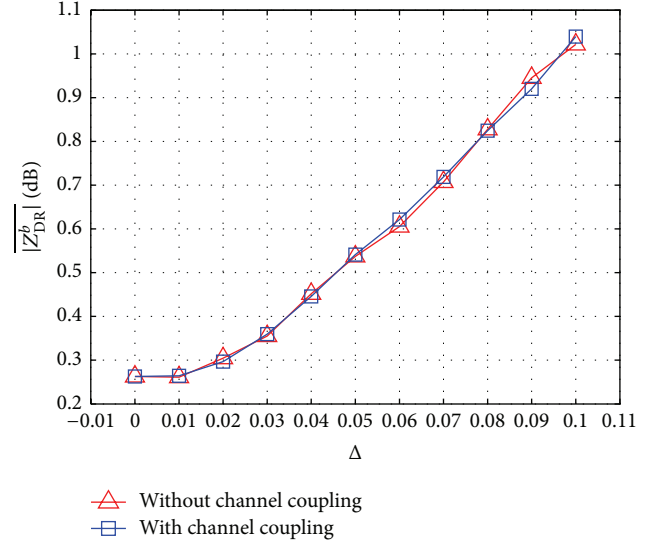
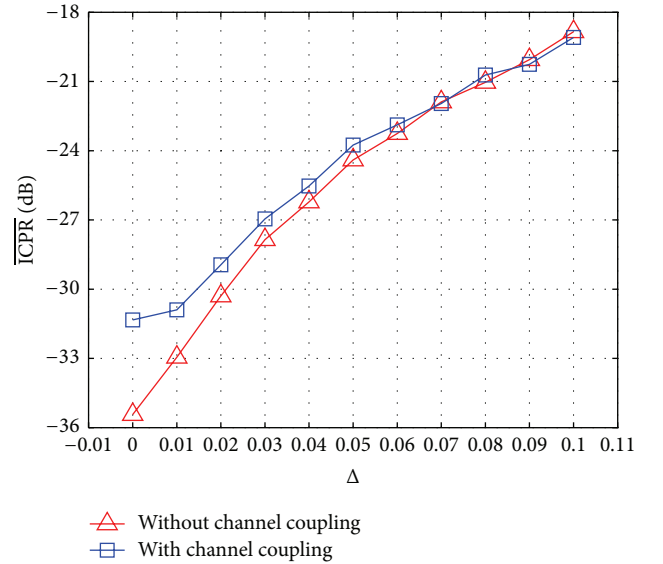
FIGURE 11: $|Z_{DR}^b|$ of a single spherical scatterer and finite beamwidth.FIGURE 12: $\overline{\text{ICPR}}$ of a single spherical scatterer and finite beamwidth.

In Figure 13 the impact of the imperfect channel isolation on Z_{DR}^b is not obvious. However, in Figure 14, the impact on ICPR is obvious when Δ is small.

4. Array Analysis in STSR Mode

In the STSR mode, the received voltages for distributed pre-cipitations are expressed as

$$\begin{aligned} & \begin{bmatrix} V_h(t) \\ V_v(t) \end{bmatrix} \\ &= \int_{\Omega} \mathbf{R}^t(\theta, \varphi) \cdot \mathbf{S}(\theta, \varphi) \cdot \mathbf{T}(\theta, \varphi) \cdot \begin{bmatrix} s_h(t) \\ s_v(t) \end{bmatrix} d\Omega, \end{aligned} \quad (46)$$

FIGURE 13: The impact of the channel coupling on $|Z_{DR}^b|$.FIGURE 14: The impact of the channel coupling on $\overline{\text{ICPR}}$.

where $s_h(t)$ and $s_v(t)$ represent two waveforms from the H and V channels. Assuming $S_{hv}(\theta, \varphi) = S_{vh}(\theta, \varphi) = 0$, (46) can be written as

$$\begin{aligned} V_h(t) &= (R_{hh}S_{hh}T_{hh} + R_{vh}S_{vv}T_{vh})s_h(t) \\ &\quad + (R_{hh}S_{hh}T_{hv} + R_{vh}S_{vv}T_{vv})s_v(t), \\ V_v(t) &= (R_{hv}S_{hh}T_{hh} + R_{vv}S_{vv}T_{vh})s_h(t) \\ &\quad + (R_{hv}S_{hh}T_{hv} + R_{vv}S_{vv}T_{vv})s_v(t). \end{aligned} \quad (47)$$

As shown in (47), $V_h(t)$ is contaminated by both the first- and second-order terms of the cross-polar patterns. In the ATSR mode, the received voltages are just contaminated by the second-order terms of the cross-polar patterns. Thus

the accuracy requirement in the STSR mode should be higher than that in the ATSR mode. As discussed in Section 3, in the ATSR mode, the relative error of the antenna pattern measurement should be under 1% to achieve $Z_{\text{DR}}^b < 0.1$ dB. Hence, the accuracy requirement in the STSR mode is more demanding.

The orthogonal waveforms are usually employed to improve the polarimetric performance [20–23]. The received voltages after passing the matched filters of the H and V channels can be written as

$$\begin{aligned} \begin{bmatrix} V_{hh}(t) & V_{hv}(t) \\ V_{vh}(t) & V_{vv}(t) \end{bmatrix} &= \begin{bmatrix} V_h(t) \otimes \tilde{s}_h(t) & V_h(t) \otimes \tilde{s}_v(t) \\ V_v(t) \otimes \tilde{s}_h(t) & V_v(t) \otimes \tilde{s}_v(t) \end{bmatrix} \\ &= \int_{\Omega} \mathbf{R}^t \cdot \mathbf{S} \cdot \mathbf{T} \cdot \begin{bmatrix} s_h(t) \otimes \tilde{s}_h(t) & s_h(t) \otimes \tilde{s}_v(t) \\ s_v(t) \otimes \tilde{s}_h(t) & s_v(t) \otimes \tilde{s}_v(t) \end{bmatrix} d\Omega, \end{aligned} \quad (48)$$

where $\tilde{s}_h(t) = g_h s_h^*(t_0 - t)$ and $\tilde{s}_v(t) = g_v s_v^*(t_0 - t)$ are the matched filters of the H and V channels, respectively. \otimes means signal convolution. If $s_h(t)$ and $s_v(t)$ are completely orthogonal, we can get

$$\begin{bmatrix} s_h(t) \otimes \tilde{s}_h(t) & s_h(t) \otimes \tilde{s}_v(t) \\ s_v(t) \otimes \tilde{s}_h(t) & s_v(t) \otimes \tilde{s}_v(t) \end{bmatrix} \propto \begin{bmatrix} 1 & 0 \\ 0 & 1 \end{bmatrix}. \quad (49)$$

In this situation, (48) is equivalent to (13) derived in the ATSR mode. Thus the same calibration procedure and analysis in Section 3 can be applied.

In practice, $s_h(t)$ and $s_v(t)$ cannot be completely orthogonal. Then we define

$$\mathbf{P}(t) = \begin{bmatrix} s_h(t) \otimes \tilde{s}_h(t) & s_h(t) \otimes \tilde{s}_v(t) \\ s_v(t) \otimes \tilde{s}_h(t) & s_v(t) \otimes \tilde{s}_v(t) \end{bmatrix}. \quad (50)$$

So (48) can be written as

$$\mathbf{V}(t) = \int_{\Omega} \mathbf{R}^t(\theta, \varphi) \cdot \mathbf{S}(\theta, \varphi) \cdot \mathbf{T}(\theta, \varphi) \cdot \mathbf{P}(t) d\Omega. \quad (51)$$

Accordingly, the calibrated voltage matrix $\hat{\mathbf{V}}(t)$ can be written as

$$\hat{\mathbf{V}}(t) = \mathbf{C}_R \cdot \mathbf{V}(t) \cdot \mathbf{P}^{-1}(t) \cdot \mathbf{C}_T, \quad (52)$$

where \mathbf{C}_T and \mathbf{C}_R are defined in (15).

Once the waveforms $s_h(t)$ and $s_v(t)$ are known, $\mathbf{P}(t)$ can be calculated from (50). Then the calibration procedure in the STSR mode is still the same as that in the ATSR mode.

5. Conclusions

In this paper, we analyze the accuracy requirements of a PPPAR in the ATSR and STSR modes. Among many factors, we focus on the polarization distortion due to the intrinsic limitation of a dual-polarized antenna element, the antenna pattern measurement error, the entire array patterns, and the imperfect H/V channels. Other factors such as the mutual coupling between the array elements are also important for the accurate weather measurement. However, these factors are ignored to simplify the analysis in this study.

The polarization distortion calibration error δ_{ij} that has the same level as the relative error upper bound E_f of the antenna pattern measurement is critical for the biases of Z_{DR} and L_{DR} . δ_{ij} should be under 0.01 to achieve $Z_{\text{DR}} < 0.1$ dB, indicating that E_f should be under 1%. The imperfect H and V channels have considerable contributions to the biases of Z_{DR} and L_{DR} . The channel isolation CIS should be over 40 dB so that the impact of the channel isolation is negligible. According to (45), the channel imbalance CIM should be under 0.05 dB to ensure $Z_{\text{DR}}^b < 0.1$ dB.

The finite beamwidth considerably affects the measurement of L_{DR} . However, the measurement of Z_{DR} is not sensitive to the finite beamwidth. Moreover, the impact of the beam scan that results in the beam expansion is just obvious on the measurement of L_{DR} . Therefore, for a large array with a narrow beam that is commonly used for weather radars, the measurement performance of Z_{DR} can be directly estimated through the measurement at the boresight, which can significantly simplify the analysis for the measurement of Z_{DR} .

In the STSR mode, if orthogonal waveforms are applied, the analysis is the same as that in the ATSR mode. Otherwise, the measurement performance may be worse than that in the ATSR mode. In the future research, those ignored factors could be taken into account to have a better understanding about the accuracy requirements of a PPPAR.

Appendix

Polarization Distortion Calibration Error

The measured element pattern \mathbf{f}_m can be expressed as

$$\mathbf{f}_m = \mathbf{f} + \mathbf{e} = \begin{bmatrix} f_{hh} & f_{hv} \\ f_{vh} & f_{vv} \end{bmatrix} + \begin{bmatrix} e_{hh} & e_{hv} \\ e_{vh} & e_{vv} \end{bmatrix}, \quad (\text{A.1})$$

where \mathbf{e} represents the absolute measurement error and \mathbf{f} is the real element pattern. It should be pointed out that the measured element pattern \mathbf{f}_m does not include the errors associated with the imperfect H and V channels which are characterized by the matrices \mathbf{A} and \mathbf{B} in (3) and (4), respectively. The matrices \mathbf{A} and \mathbf{B} are integrated in the array transmission and reception patterns to account for the bias contributions of the imperfect H and V channels. Therefore, we can just focus on the measurement error of \mathbf{f}_m .

The calibrated element pattern $\hat{\mathbf{f}}$ can be expressed as

$$\hat{\mathbf{f}} = \mathbf{f} \cdot (\mathbf{f}_m)^{-1}. \quad (\text{A.2})$$

By using the Matrix Inversion Lemma, we can get

$$(\mathbf{f}_m)^{-1} = (\mathbf{f} + \mathbf{e})^{-1} = \mathbf{f}^{-1} - \mathbf{f}^{-1} (\mathbf{f}^{-1} + \mathbf{e}^{-1})^{-1} \mathbf{f}^{-1}. \quad (\text{A.3})$$

Substituting (A.3) in (A.2), we can get

$$\hat{\mathbf{f}} = \mathbf{I} - (\mathbf{f}^{-1} + \mathbf{e}^{-1})^{-1} \mathbf{f}^{-1}, \quad (\text{A.4})$$

where \mathbf{I} is the identity matrix. Thus the polarization distortion calibration error can be written as

$$\hat{\mathbf{f}} - \mathbf{I} = \begin{bmatrix} \delta_{hh} & \delta_{hv} \\ \delta_{vh} & \delta_{vv} \end{bmatrix} = -(\mathbf{f}^{-1} + \mathbf{e}^{-1})^{-1} \mathbf{f}^{-1}. \quad (\text{A.5})$$

Equation (A.5) shows that the polarization distortion calibration error δ_{ij} is related to both the absolute measurement error \mathbf{e} and the element pattern \mathbf{f} itself.

For a well-designed antenna element, the copolar patterns are larger than the cross-polar patterns. In addition, since $|f_{ij}| \gg |e_{ij}|$, the matrix elements of \mathbf{f}^{-1} are far less than the matrix elements of \mathbf{e}^{-1} . Thus, (A.5) can be approximated as

$$\begin{aligned} \hat{\mathbf{f}} - \mathbf{I} &= -(\mathbf{f}^{-1} + \mathbf{e}^{-1})^{-1} \mathbf{f}^{-1} \approx -(\mathbf{e}^{-1})^{-1} \mathbf{f}^{-1} \\ &\approx -\mathbf{e} \cdot \mathbf{f}^{-1}. \end{aligned} \quad (\text{A.6})$$

It should be pointed out that (A.6) is only valid under the condition that the matrix elements of \mathbf{f}^{-1} are far less than the matrix elements of \mathbf{e}^{-1} . Fortunately, this condition is usually satisfied for a well-designed antenna element in the beam scan area.

Since the relative error is more essential to represent the measurement accuracy than the absolute error, we define the relative error upper bound E_f of \mathbf{e} as

$$E_f = \max_{i,j=h,v} \left\{ \frac{|e_{ij}|}{|f_{ij}|} \right\}. \quad (\text{A.7})$$

According to (A.6), the polarization distortion calibration error can be estimated as

$$\begin{aligned} \hat{\mathbf{f}} - \mathbf{I} &\approx \frac{-1}{f_{hh}f_{vv} - f_{hv}f_{vh}} \\ &\cdot \begin{bmatrix} \frac{e_{hh}}{f_{hh}}f_{hh}f_{vv} - \frac{e_{hv}}{f_{hv}}f_{hv}f_{vh} & f_{hh}f_{hv} \left(\frac{e_{hv}}{f_{hv}} - \frac{e_{hh}}{f_{hh}} \right) \\ f_{vh}f_{vv} \left(\frac{e_{vh}}{f_{vh}} - \frac{e_{vv}}{f_{vv}} \right) & \frac{e_{vv}}{f_{vv}}f_{hh}f_{vv} - \frac{e_{vh}}{f_{vh}}f_{hv}f_{vh} \end{bmatrix}. \end{aligned} \quad (\text{A.8})$$

Consequently, we can get

$$\begin{aligned} |\delta_{hh}| &\leq \frac{|f_{hh}f_{vv}| + |f_{hv}f_{vh}|}{|f_{hh}f_{vv} - f_{hv}f_{vh}|} E_f, \\ |\delta_{hv}| &\leq \frac{2|f_{hh}f_{hv}|}{|f_{hh}f_{vv} - f_{hv}f_{vh}|} E_f, \\ |\delta_{vh}| &\leq \frac{2|f_{vh}f_{vv}|}{|f_{hh}f_{vv} - f_{hv}f_{vh}|} E_f, \\ |\delta_{vv}| &\leq \frac{|f_{hh}f_{vv}| + |f_{hv}f_{vh}|}{|f_{hh}f_{vv} - f_{hv}f_{vh}|} E_f. \end{aligned} \quad (\text{A.9})$$

For a well-designed antenna element, (A.9) reveals that E_f and $|\delta_{ij}|$ are at the same level. Thus we just focus on the polarization distortion calibration error δ_{ij} in this paper. When we need to focus on a specific array, the analysis herein can be applied.

Conflict of Interests

The authors declare that there is no conflict of interests regarding the publication of this paper.

Acknowledgments

This work was supported by the National Natural Science Foundation of China under Grant nos. 61201330, 61490690, and 61490694. The authors sincerely express their gratitude to the anonymous reviewers.

References

- [1] G. Zhang, R. J. Doviak, D. S. Zrnic, J. Crain, D. Staiman, and Y. Al-Rashid, "Phased array radar polarimetry for weather sensing: a theoretical formulation for bias corrections," *IEEE Transactions on Geoscience and Remote Sensing*, vol. 47, no. 11, pp. 3679–3689, 2009.
- [2] R. H. Medina, E. J. Knapp, J. L. Salazar, and D. J. McLaughlin, "T/r module for casa phase-tilt radar antenna array," in *Proceedings of the 7th European Microwave Integrated Circuits Conference (EuMIC '12)*, pp. 913–916, IEEE, October 2012.
- [3] C. Fulton and W. Chappell, "A dual-polarized patch antenna for weather radar applications," in *Proceedings of the IEEE International Conference on Microwaves, Communications, Antennas and Electronic Systems (COMCAS '11)*, pp. 1–5, November 2011.
- [4] C. Fulton and W. J. Chappell, "Calibration of a digital phased array for polarimetric radar," in *Proceedings of the IEEE MTT-S International Microwave Symposium Digest (MTT '10)*, pp. 161–164, IEEE, May 2010.
- [5] G. Zhang, R. J. Doviak, D. S. Zrnić, R. Palmer, L. Lei, and Y. Al-Rashid, "Polarimetric phased-array radar for weather measurement: a planar or cylindrical configuration?" *Journal of Atmospheric and Oceanic Technology*, vol. 28, no. 1, pp. 63–73, 2011.
- [6] C. Fulton, G. Zhang, W. Bocangel, L. Lei, R. Kelley, and M. McCord, "Cylindrical Polarimetric phased array radar: a multi-function demonstrator and its calibration," in *Proceedings of the IEEE International Conference on Microwaves, Communications, Antennas and Electronic Systems (COMCAS '13)*, pp. 1–5, October 2013.
- [7] M. Sánchez-Barbety, R. W. Jackson, and S. Frasier, "Interleaved sparse arrays for polarization control of electronically steered phased arrays for meteorological applications," *IEEE Transactions on Geoscience and Remote Sensing*, vol. 50, no. 4, pp. 1283–1290, 2012.
- [8] J. Dong, Q. Liu, and X. Wang, "New polarization basis for polarimetric phased array weather radar: theory and polarimetric variables measurement," *International Journal of Antennas and Propagation*, vol. 2012, Article ID 193913, 15 pages, 2012.
- [9] D. Zrnić, R. Doviak, G. Zhang, and A. Ryzhkov, "Bias in differential reflectivity due to cross coupling through the radiation patterns of polarimetric weather radars," *Journal of Atmospheric and Oceanic Technology*, vol. 27, no. 10, pp. 1624–1637, 2010.
- [10] V. Chandrasekar and R. J. Keeler, "Antenna pattern analysis and measurements for multiparameter radars," *Journal of Atmospheric & Oceanic Technology*, vol. 10, no. 5, pp. 674–683, 1993.
- [11] D. N. Moiseev, C. M. H. Unal, H. W. J. Russchenberg, and L. P. Ligthart, "Improved polarimetric calibration for atmospheric radars," *Journal of Atmospheric and Oceanic Technology*, vol. 19, no. 12, pp. 1968–1977, 2002.

- [12] Y. Wang and V. Chandrasekar, "Polarization isolation requirements for linear dual-polarization weather radar in simultaneous transmission mode of operation," *IEEE Transactions on Geoscience and Remote Sensing*, vol. 44, no. 8, pp. 2019–2028, 2006.
- [13] M. Galletti and D. S. Zrnic, "Bias in copolar correlation coefficient caused by antenna radiation patterns," *IEEE Transactions on Geoscience and Remote Sensing*, vol. 49, no. 6, pp. 2274–2280, 2011.
- [14] C. Fulton, J. Herd, S. Karimkashi, G. Zhang, and D. Zrnic, "Dual-polarization challenges in weather radar requirements for multifunction phased array radar," in *Proceedings of the 5th IEEE International Symposium on Phased Array Systems and Technology (ARRAY '13)*, pp. 494–501, October 2013.
- [15] D. S. Zrnic, G. Zhang, and R. J. Doviak, "Bias correction and doppler measurement for polarimetric phased-array radar," *IEEE Transactions on Geoscience and Remote Sensing*, vol. 49, no. 2, pp. 843–853, 2011.
- [16] L. Lei, G. Zhang, and R. J. Doviak, "Bias correction for polarimetric phased-array radar with idealized aperture and patch antenna elements," *IEEE Transactions on Geoscience and Remote Sensing*, vol. 51, no. 1, pp. 473–486, 2013.
- [17] A. Ludwig, "The definition of cross polarization," *IEEE Transactions on Antennas and Propagation*, vol. 21, no. 1, pp. 116–119, 1973.
- [18] J. L. Salazar, R. H. Medina, and E. Loew, "T/R modules for active phased array radars," in *Proceedings of the IEEE International Radar Conference (RadarCon '15)*, pp. 1125–1133, Arlington, Va, USA, May 2015.
- [19] C. Fulton and W. Chappell, "Calibration of panelized polarimetric phased array radar antennas: a case study," in *Proceedings of the 4th IEEE International Symposium on Phased Array Systems and Technology (ARRAY '10)*, pp. 860–867, October 2010.
- [20] D. Giuli, M. Fossi, and L. Facheris, "Radar target scattering matrix measurement through orthogonal signals," *IEEE Proceedings, Part F: Radar and Signal Processing*, vol. 140, no. 4, pp. 233–242, 1993.
- [21] O. A. Krasnov and L. P. Ligthart, "Radar polarimetry using sounding signals with dual orthogonality-PARSAX approach," in *Proceedings of the 7th European Radar Conference (EuRAD '10)*, pp. 121–124, September 2010.
- [22] G. Galati, G. Pavan, and S. Scopelliti, "MPAR: waveform design for the weather function," in *Proceedings of the European Radar Conference (EuRAD '10)*, pp. 152–155, IEEE, Paris, France, October 2010.
- [23] Z. Wang, F. Tigrek, O. Krasnov, F. van der Zwan, P. van Genderen, and A. Yarovoy, "Interleaved OFDM radar signals for simultaneous polarimetric measurements," *IEEE Transactions on Aerospace and Electronic Systems*, vol. 48, no. 3, pp. 2085–2099, 2012.

